RSC Advances

PAPER

View Article Online
View Journal | View Issue

Cite this: *RSC Adv.*, 2025, **15**, 31498

Thermal annealing modulates the structural, optical, and antibacterial properties of Cu-based nanoparticles

Ferid Ben Nasr, *[a] Hajer Jlidi, [b] Wahida Ltaief,[a] Sami Mnif,[b] Hajer Guermazi, [a] Samir Guermazi,[a] Benoît Duponchel,[c] Gérard Leroy[c] and Sami Aifa[b]

Numerous studies have demonstrated the antiproliferative potential of copper-based nanoparticles (Cu-based NPs) in antibacterial and anticancer applications. This study investigates how thermal annealing influences the structural, optical, and antibacterial properties of Cu-based NPs. X-ray diffraction (XRD) analysis revealed a monoclinic $Cu_4SO_4(OH)_6$ phase for the as-prepared powder, and monoclinic CuO phase after annealing, alongside a notable increase in crystallite size from 8.20 nm to 30.20 nm. Optical characterization shows a reduction in the band gap, a decrease in Urbach energy and an increase in the steepness parameter as a result of annealing, confirming improved crystallinity. Interestingly, the as-synthesized $Cu_4SO_4(OH)_6$ phase exhibits higher antibacterial activity (MIC = 0.31 – 2.5 mg mL^{-1}) compared to the annealed particles, likely due to its higher specific surface area (114.16 m^2 g^{-1} *vs.* 29.58 m^2 g^{-1}) and unique crystal morphology. Both materials exhibit dose-dependent anti-adhesive effects against MRSA (>70% inhibition at 5 mg mL^{-1}), and the intermediate phase shows enhanced efficacy at higher concentrations. These results underscore the critical role of thermal processing in tailoring material properties while revealing the unexpected antimicrobial potential of non-annealed copper based nanoparticles.

Received 13th June 2025
Accepted 18th August 2025

DOI: 10.1039/d5ra04198h

rsc.li/rsc-advances

1. Introduction

The characteristics of inorganic materials are significantly influenced by their shapes, sizes, and crystallographic structures, prompting extensive research aimed at developing nano- and micro-scale inorganic materials with unique and distinctive morphologies.[1] Copper oxide (CuO), an important p-type metal oxide semiconductor with a narrow band gap of 1.8–2.5 eV,[2] has gained a leading edge in various applications,[3] including catalysis,[4] gas sensing,[5] and antibacterial uses.[6] Recently, nanoparticles (NPs) have become increasingly prevalent across diverse fields, with metal oxide NPs, in particular, emerging as a prominent area within nanotechnology due to their potential in addressing microbial infections.

Copper-based nanoparticles (CuNPs) have demonstrated broad-spectrum antibacterial activity against Gram-positive and Gram-negative microorganisms. Notably, their antibacterial effect does not require specific UV activation, highlighting their potential as versatile agents for controlling bacterial infections.[7] Similarly, activated carbon fiber (ACF) filters coated with silver NPs effectively inhibit bacterial growth, particularly against *Bacillus subtilis* and *Escherichia coli*, showcasing their utility in antimicrobial applications.[7] Copper nanoparticles have also exhibited remarkable antimicrobial properties. The mechanisms behind copper's toxicity include membrane rupture, ion accumulation, protein inactivation, and DNA damage, making CuO an important material for combating bacterial and viral infections.[7]

Furthermore, CuONPs have been found to induce autophagy-related cytotoxicity in A549 cells, demonstrating their toxicity *via* the autophagic biomarker LC3-II, and this effect can be mitigated using autophagy inhibitors.[7] Copper nanoparticles synthesized through the modified polyol method exhibited higher antimicrobial activity against *Escherichia coli* compared to *Candida albicans*.[7] In catalytic applications, CuO-based catalysts have gained attention for their role in advanced oxidation processes (AOPs), offering high activity, stability, and environmental friendliness.[7] Meanwhile, silver NPs are extensively used in medical diagnostics and therapies due to their unique properties, although biological methods of synthesis are preferred to reduce the toxic byproducts associated with chemical methods.[7]

This integrated understanding of the antibacterial and catalytic potential of CuO, ZnO, and silver NPs highlights their growing importance in antimicrobial technologies and

[a]*Laboratory of Materials for Energy and Environment, and Modeling, University of Sfax, Faculty of Sciences, B.P:1171, 3000 Sfax, Tunisia. E-mail: fd.bennasr@gmail.com*

[b]*Laboratory of Molecular and Cellular Screening Processes, Centre of Biotechnology of Sfax, P.O. Box 1177, 3018 Sfax, Tunisia*

[c]*Units of Dynamic and Structure of Molecular Materials (UDSMM), Littoral Côte-d'Opale University, Centre de La Mi-Voix, 62228 Calais, France*

industrial applications. Our previous work demonstrated that the reaction between $CuSO_4$, $5H_2O$ and NaOH produces CuO upon annealing, with diffraction analysis revealing a secondary phase potentially contributing to antibacterial activity.[8]

In the following sections, we detail the synthesis of Copper-based nanoparticles (CuNPs) both before and after annealing, along with their structural and spectroscopic characterization. We evaluate their antibacterial properties against various bacterial strains, focusing on the relationship between structural modifications induced by annealing and antibacterial efficacy. This study aims to enhance our understanding of how thermal treatment affects the antimicrobial potential of CuNPs, thereby advancing the application of metal oxide NPs in relevant fields.

While most studies focus on copper oxide (CuO) nanoparticles, this work explores for the first time the antimicrobial potential of an intermediate hydroxysulfate phase. To our knowledge, the $Cu_4SO_4(OH)_6$ phase has not been extensively studied for its antibacterial properties.

2. Material and methods

2.1. Synthesis

The synthesis of nanopowders was carried out using a precipitation method. Copper(II) sulfate pentahydrate ($CuSO_4$, $5H_2O$) was employed as the precursor. Initially, a specific mass of copper sulfate was dissolved in 50 mL of distilled water under magnetic stirring at room temperature for 15 minutes. The pH of the solution was adjusted to a range of 11–12 by gradually adding a 1M NaOH (sodium hydroxide) solution dropwise. This step led to the formation of a blue precipitate. After filtration, the precipitate was washed several times with distilled water and ethanol to remove impurities. It was then dried at 80 °C for 12 hours (denoted as S_1).

Alternatively, a portion of the precipitate was annealed at 350 °C for 4 hours, ground again, and subsequently calcined at 600 °C for 12 hours to obtain the final powder (denoted as S_2).[8]

All chemical reagents, such as the primary precursor ($CuSO_4$, $5H_2O$), along with (NaOH), distilled water, and ethanol, were sourced from Sigma Aldrich (purity >99%).

2.2. Characterization methods

Morphological characterization was performed using a scanning electron microscope (JEOL JSM7100F) coupled with an energy dispersive spectrometer (EDS) for elemental composition analysis. X-ray diffraction (XRD) patterns were obtained using a Bruker D8Advance diffractometer with monochromated CuK_α radiation ($\lambda = 1.5406$ Å). Infrared spectra were recorded in the 4000–400 cm^{-1} range using a PerkinElmer FT-IR spectrometer. Optical absorption was measured with a PerkinElmer UV-vis Lambda 365 spectrophotometer in the 190–1100 nm wavelength domain.

2.3. Preparation of strains and NPs for the study of antibacterial activity

Gram-positive bacteria *Staphylococcus aureus* ATCC33591, and *Staphylococcus epidermidis* S61, along with Gram-negative bacteria *Escherichia coli*, *Pseudomonas aeruginosa* and *Serratia* sp., were cultured in Muller Hinton broth (MHB) medium for 16–24 hours at 30 °C.[9] The optical densities of the cultures were then adjusted with liquid MHB medium to achieve a concentration of $1–5 \times 10^8$ CFU mL^{-1} for each bacterium.[10,11] To assess antibacterial activity, NPs were treated in an ultrasonic bath for 30 minutes.[12,13]

2.4. Micro-dilution tests

The antibacterial activity was assessed using the micro-dilution technique. MIC values were determined using a 96-wellmicroplate following the protocol described by.[14] Briefly, NPs were put in wells containing MHB medium and then, two-fold dilution series were prepared in the 96-well micro-plate. The micro-titer plates were then incubated at 30–37 °C for 24 h and the reading was taken after exposing each well to 20 μL MTT (3- (4, 5-dimethylthiazol-2-yl) – 2,5- diphenyl-tetra-zolium-bromide) at a concentration of 0.5 mg mL^{-1}. The viability of bacteria is detected by the appearance of a blue-violet coloration. The MIC value is deduced from the last well without bacterial growth hand the first well with growth. After incubation and revelation with MTT, 10 μL were taken from each well, which didn't show an apparent growth and plated on solid LB medium by streaking. The Petri dishes were incubated for 24 h, and the bacterial growth was assessed.

2.5. Antibiofilm activity

The anti-biofilm activities of both annealed and non-annealed (Cu NPs) were evaluated against *Staphylococcus aureus* ATCC33591, a strain known for its ability to form biofilms and its resistance to methicillin.[15] The assessment of anti-adherence properties was conducted using 96-well flat-bottom microtiter plates, following a modified protocol based on.[6] Solutions of Cu NPs, prepared in Tryptone Soy Broth (TSB), were subjected to ultrasonic treatment for one hour at 25 °C. A 100 μl aliquot of these solutions was added to the first column of the plates, followed by a serial two-fold dilution across the wells. Subsequently, 50 μl of glucose was added to each well, achieving a final concentration of 2.25% (w v^{-1}). An overnight culture of *S. aureus* was prepared in TSB at 37 °C and diluted appropriately to achieve a final optical density (OD) of 0.1 at 600 nm when inoculated into all wells. Control wells contained TSB without NPs. After a 24-hours incubation at 37 °C, the TSB and planktonic cells were discarded, and the wells were washed twice with 200 mL of sterile phosphate-buffered saline (PBS) (pH = 7.2). The plates were then dried at 60 °C for one hour. Each well received 150 mL of 0.2% crystal violet solution (w per v in 20% ethanol) for staining, followed by rinsing three times with water to remove excess dye. To solubilize the biofilm, 200 mL of glacial acetic acid (33% v/v) was added to each well and incubated for one hour at room temperature. Finally, the optical density was measured at a wavelength of 570 nm using a microplate reader. The percentage of biofilm inhibition was calculated by comparing the absorbance values of untreated *versus* treated biofilms.

$$\%\ \text{biofilm inhibition} = \frac{(OD_{570\text{control}} - OD_{570\text{treated}})}{OD_{\text{control}}} \times 100 \quad (1)$$

2.6. Statistical analysis

Antibacterial activity tests were performed in biological duplicates $n = 2$ for each tested bacterial strain and condition (S_1 and S_2), the minimum inhibitory concentration (MIC) values were reported as mean ± standard deviation.

Antiadhesive activity was assessed in replicates ($n = 4$). The results are expressed as mean ± standard deviation. For each tested condition, the standard deviation was calculated and used to generate error bars in bar graphs. All calculations were performed using Microsoft Excel (version 2506).

3. Results and discussion

3.1. Energy dispersive spectroscopy (EDS) analysis

To examine the chemical elements and assess the purity of the synthesized powders, we conducted an analysis of the obtained samples using the Energy Dispersive Spectroscopy (EDS) technique.

The variation in intensity [cps eV^{-1}] as a function of energy [keV] (Fig. 1), allowed us to identify the chemical elements present within the synthesized samples.

The EDS analysis of the compounds S_1 and S_2 reveals the presence of oxygen, copper, and sulfur in varying intensities, indicating their relative abundances. The energy peaks at 0.5 keV for oxygen and at 0.8 keV for copper, with respective intensities of 14 Cps eV^{-1} and 16 Cps eV^{-1}, confirm that copper is the main constituent of the samples, while sulfur is present in lesser amounts at 2.3 keV with an intensity of 4 Cps eV^{-1}. Additionally, the peaks at higher energies (8 keV and 8.9 keV) for copper suggest deeper electronic transitions, although their intensity is relatively low. These results highlight the importance of oxygen and copper in the composition of the compounds, providing essential information for understanding their physical and chemical properties in various applications, such as catalysis or electronic devices.

The elemental composition was presented as a table in the inset of each figure. The shift from the predicted values is due to defects such as oxygen vacancies and/or Cu interstitial.

3.2. X-ray diffraction study

To assess phase identification and crystallinity of the synthesized powders, X-ray diffraction (XRD) analysis was conducted. The XRD patterns are presented in Fig. 2.

Notably, the XRD patterns of the two samples exhibit multiple diffraction peaks consistent with ICCD card no.: 96-200-6545 of $Cu_4SO_4(OH)_6$ phase for S_1,[16] and ICCD card no. 00-045-0937 of CuO phase for S_2.[17] These diffraction patterns can easily be associated with the monoclinic crystal structures having the $P2_1/c$ and $C2/c$ space group, for S_1 and S_2 respectively.

Although moderately intense, the (−202) peak at 42.77° and (−125) peak at 46.46° serve as structural markers for the S_1 and S_2 phases, respectively. The (−125) peak exclusive presence in S_1 provides unambiguous phase identification, and its partial decrease after annealing directly tracks the structural transformation to S_1. While the lower intensity presented analytical challenges, this interpretation is robustly supported by correlated FTIR sulfate vibrations (Fig. 4).

The (−202) peak exclusive presence in S_2 along with other characteristic ((200) (002)) are the markers of the monoclinic CuO purity according to ICCD card no. 00-045-0937.

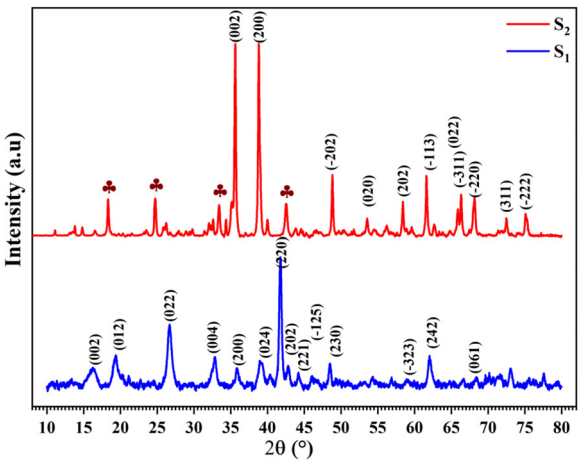

Fig. 2 XRD patterns of S_1 and S_2 powders.

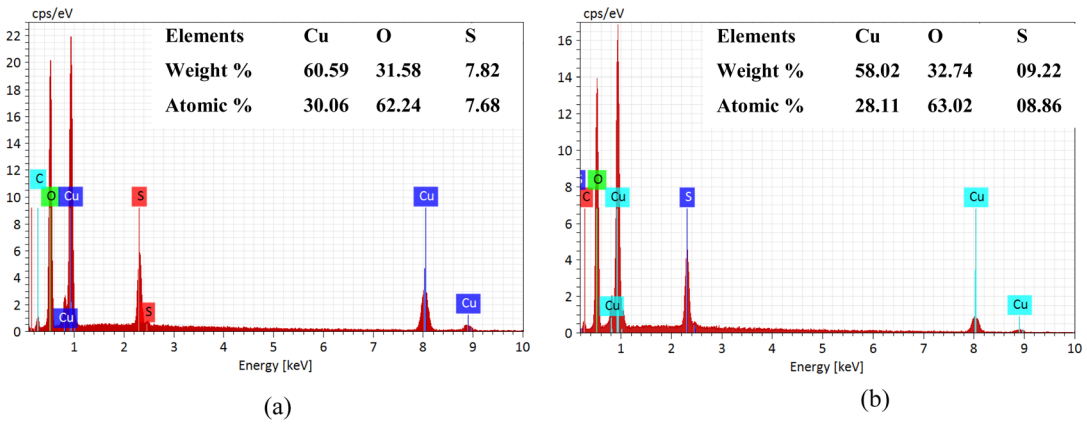

Fig. 1 EDS spectra of (a): S_1, (b): S_2.

In fact, in the first step of the synthesis process, sulphate pentahydrate ($CuSO_4$, $5H_2O$) initially reacts with NaOH to form the blue precipitate of $Cu_4SO_4(OH)_6$ *via* a simple chemical reaction:

$$4(CuSO_4{,}5H_2O) + 6NaOH\ Cu_4SO_4(OH)_6 + 3Na_2SO_4 + 20H_2O \quad (2)$$

After annealing at 600 °C for 12 hours we obtain the final powder as follows:

$$Cu_4SO_4(OH)_6\ 4\ CuO + SO_3 + 3H_2O \quad (3)$$

XRD and microstructural analysis reveal a conversion of $S_1$to S_2 through annealing at 600 °C for 12 hours.[18] Despite the thermal treatment, the XRD pattern of the annealed compound (S_2) still exhibit additional characteristic diffraction peaks (marked with ♣ symbols), confirming the persistence of the $Cu_4SO_4(OH)_6$ crystalline phase after annealing.

The structure of S_1, characterized by large lattice parameters ($a = 5.03$ Å, $b = 8.50$ Å, $c = 11.02$ Å, $\beta = 96.48°$ and $V = 468.51$ Å^3) and a high specific surface area (114.16 m^2 g^{-1}), evolves into a more compact CuO phase ($a = 4.57$ Å, $b = 3.42$ Å, $c = 5.10$ Å, $\beta = 99.26°$ and $V = 78.67$ Å^3) with higher density (6.71 g cm^{-3}) (Table 1).

For additional structural investigations, micro-structural parameters were calculated and analyzed. The lattice constants (a, b and c) were calculated using the following formulas:[19]

$$2d_{hkl}\sin(\theta) = n\lambda \quad (4)$$

For monoclinic S_1 and S_2:

$$\frac{1}{d_{hk\ell}{}^2} = \frac{1}{\sin^2(\beta)}\left[\frac{h^2}{a^2} + \frac{k^2\sin^2(\beta)}{b^2} + \frac{\ell^2}{c^2} - \frac{2h\ell\cos(\beta)}{ac}\right] \quad (5)$$

Moreover, the unit cell volume V, for the monoclinic S_1 and S_2, is given by

$$V = abc\ \sin(\beta) \quad (6)$$

The calculated values of structural parameters are gathered in Table 1.

Table 1 Structural and micro structural parameters of S_1 and S_2 samples

Samples	S_1	S_2
a (Å)	5.03	4.57
b (Å)	8.50	3.42
c (Å)	11.02	5.10
β (°)	96.48	99.26
V (Å^3)	468.51	78.67
D (nm)	8.20	30.2
ε	-5.16×10^{-3}	-8.03×10^{-4}
δ (line nm^{-2})	1.88×10^{-2}	8.73×10^{-4}
ρ (g cm^{-3})	6.41	6.71
SSA(m^2 g^{-1})	114.16	29.58

The average crystallite size (D) and micro-strain (ε) of the prepared samples are estimated from the measured full width at half maximum (FWHM) of the XRD peaks using Williamson–Hall (W–H) model[20]

$$\beta_{hk\ell}\cos\theta = \frac{k\lambda}{D} + 4\varepsilon\sin\theta \quad (7)$$

The W–H plots (Fig. 3) permit the evaluation of micro-strain from the slope of the fit and crystallite size from the intercept with the y-axis.

Then, the dislocation density (δ) was deduced using this relation:[21]

$$\delta = \frac{15\varepsilon}{aD} \quad (8)$$

The specific surface area (SSA) plays a crucial role in the antibacterial activities of the NPs, as it defines the contact surface with the surrounding molecules. The (SSA) can be estimated using the following relations:[22]

$$SSA = \frac{6}{D \times \rho} \quad (9)$$

$$\rho = \frac{Z \times M}{N \times V} \quad (10)$$

Both materials exhibit compressive microstrain, though significantly reduced in S_2 compared to S_1 (Table 1). This strain relaxation stems from: phase transformation-induced volume contraction, thermal defect annihilation during annealing, and crystallite coarsening (8.2 to 30.2 nm). The retained compressive strain in S_2 suggests interfacial stresses from incomplete phase conversion, while S_1's higher strain correlates with its enhanced surface reactivity and superior antibacterial performance.

The large SSA of the S_1 NPs will directly and significantly improve its antibacterial activity. Biological tests are required to validate this hypothesis.

3.3. Fourier transform infrared (FTIR) study

Room-temperature FTIR spectroscopy [400–4000] cm^{-1} reveals distinct vibrational signatures for the S_1 and S_2 phases, as shown in Fig. 4.

The FTIR results for the two compounds reveal significant differences that reflect their structures and chemical transformations. For S_1 before annealing, the bands observed at 468, 483, and 510 cm^{-1} are typical of Cu–O bond vibrations (Fig. 4b). Peaks around 596, 629, and 732 cm^{-1} correspond to sulfate ($SO_4{}^{-2}$) group vibrations, while those at 779, 848, and 872 cm^{-1} can be attributed to hydroxyl group (OH) vibrations or combined modes with sulfate groups. The bands at 942, 984, 1085, and 1119 cm^{-1} also indicate sulfate group vibrations.

The bands at 3386, 3567, and 3589 cm^{-1} correspond to hydroxyl stretching vibrations. The broad band at 3386 cm^{-1} is assigned to adsorbed H_2O on the particle surface.[23] While the

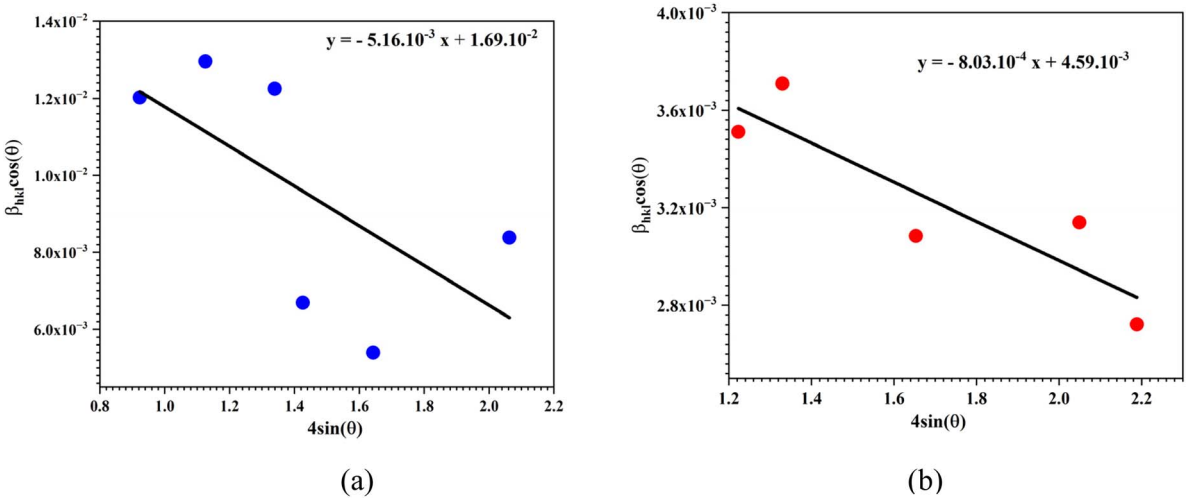

Fig. 3 Williamson–Hall (W–H) plot for (a): S_1, (b): S_2.

sharper bands at 3567 and 3589 cm^{-1} are attributed to structural OH groups in the sample, consistent with hydroxo-bridged Cu(II) complexes[24] and layered hydroxy sulfate minerals like brochantite.[25]

After annealing, S_2 shows distinct bands: peaks at 416 and 480 cm^{-1} are characteristic of Cu–O bond vibrations in copper(II) oxide. The bands in the region 598–1257 cm^{-1}, confirm the presence of $Cu_4SO_4(OH)_6$ phase. These observations confirm that annealing has transformed partially the $Cu_4SO_4(OH)_6$ phase to CuO.

3.4. Surface morphology

SEM images in Fig. 5 showed the morphologies of the two samples S_1 and S_2. We observed agglomerated particles of various shapes and sizes, depending on annealing. The observed agglomerations can be due to the OH groups present on the surface of the NPs,[6] as proved by FTIR analysis. It is clear that annealing leads to significant morphological changes of particles, which can seriously affect their reactive surfaces and thus their antibacterial efficacy. It is noteworthy that the S_1 NPs ($Cu_4SO_4(OH)_6$) have a nanorods shape, while the annealing leads to largest mico-particle size distribution. Nanorod particles are expected to show the greatest antibacterial effectiveness.

4. Antibacterial test

The antibacterial efficacy of both annealed and non-annealed nanopowders was evaluated by determining their Minimum Inhibitory Concentration (MIC) and Minimum Bactericidal Concentration (MBC) against Gram-positive (*Staphylococcus epidermidis* and *Staphylococcus aureus*) and Gram-negative (*Escherichia coli*, *Pseudomonas aeruginosa* and *Serratia* sp) bacteria. The MIC and MBC values, which are crucial indicators of antibacterial effectiveness, are summarized in Table 2. The MIC values ranged from 0.31 to 2.5 mg mL^{-1}. Overall, the S_1

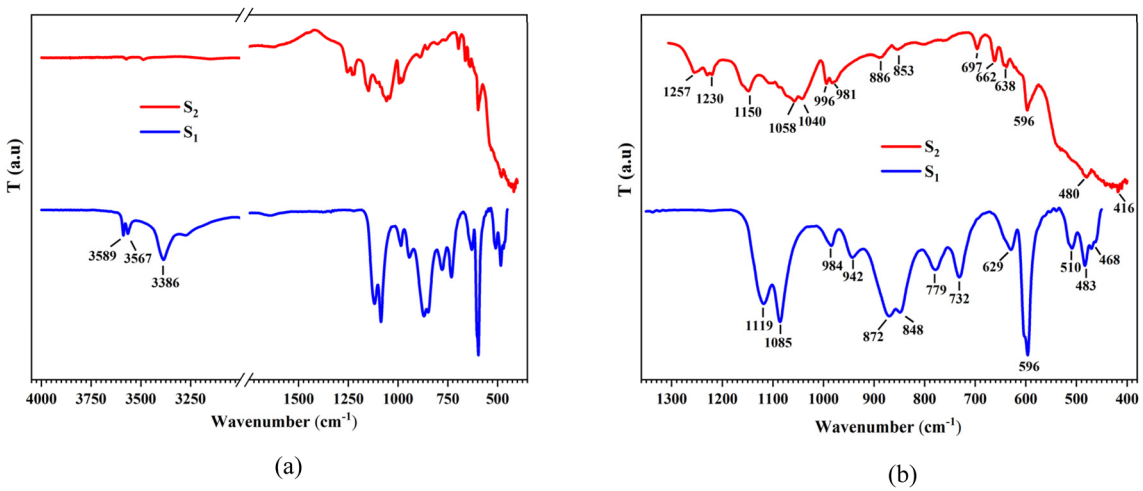

Fig. 4 FTIR spectra of S_1 and S_2 NPs in (a): 400–4000 cm^{-1} and (b) enlarged 400–1400 cm^{-1} region.

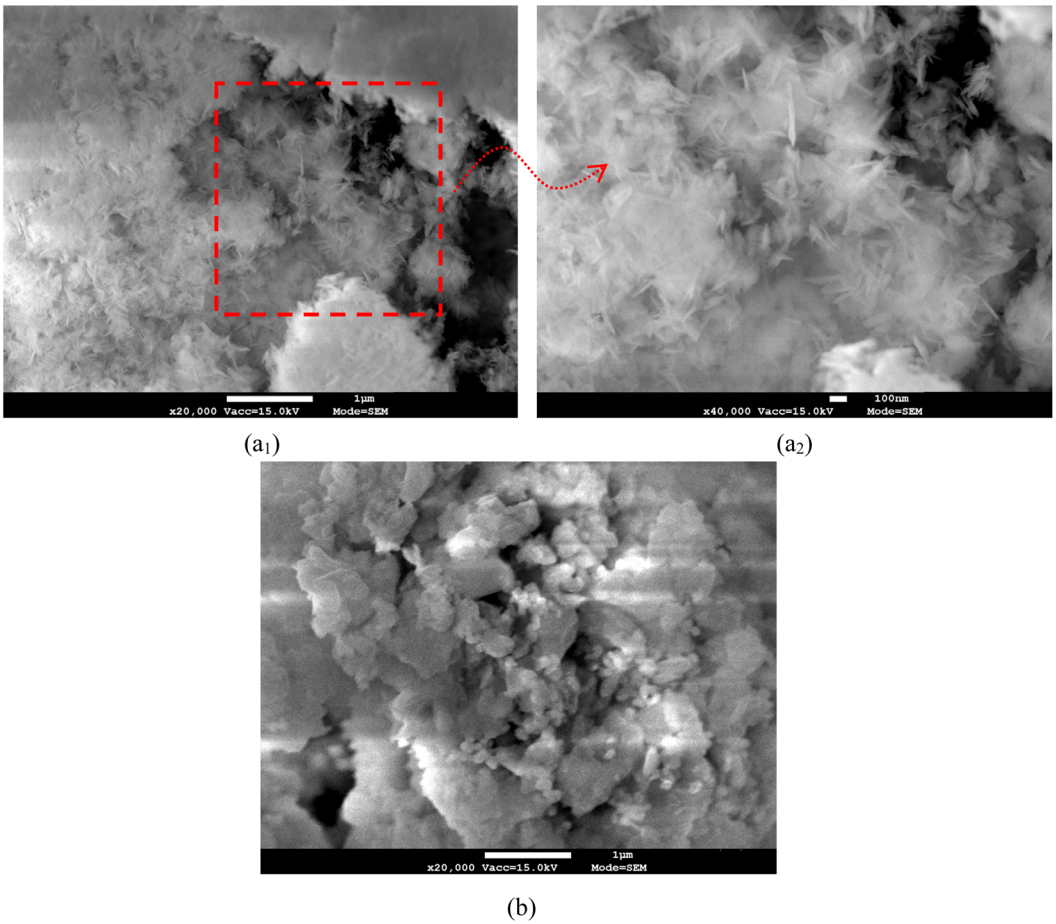

Fig. 5 SEM images of (a_1 and a_2): S_1 at different magnifications, and (b): S_2.

nanopowders exhibited greater antibacterial activity, displaying lower MIC values compared to their S_2 counterparts. Specifically, all MIC values obtained with the S_1 nanopowders were equal to or lower than those of the S_2, suggesting enhanced activity of the S_1 intermediate phase. This trend was also partially observed with the MBC values.

Annealing not only influences antibacterial activity by changing the specific surface area and altering physico-chemical characteristics, but also plays a role in modulating the release of essential ions (*e.g.*, Cu^{2+}).

Based on these findings, we conclude, for the first time, that the intermediate phase (S_1) demonstrates more promising antibacterial potential than the CuO NPs obtained after annealing. Azam *et al.* Reported that nanoparticle size influences antibacterial activity and is related to annealing temperature.[7] A correlation between size and activity cannot be determined due to the heterogeneity of the size resulting from the presence of various impurities.[8] In our case, S_1 presented an average of SSA more important than S_2 NPs which could justify its important antibacterial activity. In fact, the surface area of NPs (SSA) is a critical factor in determining their antibacterial activity. A larger surface area facilitates more effective interactions between the NPs and bacterial cell membranes, promoting the delivery of antimicrobial agents or the

Table 2 (MIC) and (MBC) values, obtained with NPs against Gram-positive and Gram negative bacterial strains[a]

		S_1			S_2		
	Strains	MIC (mg mL^{-1})	MBC (mg mL^{-1})	MBC MIC	MIC (mg mL^{-1})	MBC (mg mL^{-1})	MBC IC
Gram(+)	*Staphylococcus epidermidis*	0.62 ± 0.21	2.5	4.03	0.62 ± 0.0	5	8.06
	Staphylococcus aureus	0.31 ± 0.0	2.5	8.06	1.25 ± 0.0	2.5	2
Gram(−)	*Escherichia coli*	0.62 ± 0.21	>10	N.A	1.25 ± 0.88	>10	N.A
	Pseudomonas aeruginosa	2.5 ± 0.0	>10	N.A	2.5 ± 0.88	>10	N.A
	Serratia sp.	0.31 ± 0.21	10	32.25	0.62 ± 0.0	10	16.12

[a] N.A: not applicable.

disruption of bacterial cell integrity.[26] NPs with increased surface area also possess a higher density of binding sites, enhancing their attachment to bacterial cell surfaces and enabling more efficient penetration through biofilms, which are often resistant to conventional antibiotics.[27] The antibacterial activity of nano-metal oxides is partly due to the production of oxygen species such as H_2O_2 that inhibits bacterial growth.[28] CuO NPs are highly absorbent, adsorbent penetrating and readily available antibiofilm agents.[29]

Our results conclusively demonstrate that the intermediate phase (S_1) exhibits superior antimicrobial properties compared to both annealed (S_2) and other copper-based nanomaterials reported in the literature. Antibacterial activity tests reveal that S_1 has significantly lower MIC values (0.31–2.5 mg mL^{-1}) than S_2.

NPs of smaller size are known to be more reactive due to their larger specific surface area.[30] Ultra-small synthesized CuO NPs showed spherical morphology, 7 and 14 nm particle sizes and inhibit bacterial growth at MIC values of 2.50 to 3.75 mg mL^{-1}.[31] These results may explain the better antibacterial activity of S_1 (8.2 nm) compared to S_2 (30.2 nm). More performant antibacterial was reported with 20–75 μg mL^{-1} of MIC values[32] despite the more important size of NPs (20–27 nm). Green synthesis CuONPS produced 30.9 nm to 10.7 nm CuONPS sizes with weak MIC values (62.5 to 125 μg mL^{-1}), compared to our S_1, against clinical isolates, including same bacteria species such as *Staphylococcus aureus* (MRSA), *Escherichia coli* and *Pseudomonas aeruginosa*.[33] The more important efficacy of S_1 may be explained by three key structural features of S_1, first a high specific surface area (114.16 $m^2\ g^{-1}$ *vs.* 29.58 $m^2\ g^{-1}$ for S_2), second optimized Cu^{2+} ion release kinetics and the presence of sulfate groups that enhance membrane disruption.

In this context, copper oxide (CuO) NPs exhibit potent antibacterial activity through several well-established mechanisms. Primarily, they generate reactive oxygen species (ROS) that induce oxidative stress, damaging bacterial membranes, proteins, and DNA. Additionally, CuO NPs release copper ions (Cu^{2+}) which disrupt essential enzymatic functions and bacterial metabolism. Their nanoscale size and surface properties facilitate direct interaction with bacterial cell walls, causing physical membrane disruption and increased permeability. Studies also highlight that the NPs' hydrodynamic diameter and surface charge critically influence their membrane penetration and antibacterial potency. These multifaceted antibacterial actions make CuO NPs promising alternatives to conventional antibiotics, with demonstrated activity against pathogens like *Staphylococcus aureus*, *Escherichia coli*, and *Pseudomonas aeruginosa*.[34]

5. Antibiofilm activity

The anti-adhesive activity of annealed and non-annealed nanoparticles (NPs) was evaluated against *Staphylococcus aureus* MRSA ATCC33591 (Fig. 6). Both nanopowders showed comparable antibiofilm activity, with no statistically significant differences across tested concentrations. At 5 mg mL^{-1}, both achieved over 70% inhibition, confirming dose-dependent efficacy. Notably, non-annealed NPs exhibited slightly higher activity at elevated concentrations, while annealed NPs were more effective at lower doses (≤0.156 mg mL^{-1}).

X-ray diffraction (XRD) analysis revealed that annealing preserved the monoclinic phase for both $Cu_4SO_4(OH)_6$ and CuO. This suggests that the observed differences in anti-adhesive activity are primarily attributed to changes in crystallite size rather than phase transitions, as the monoclinic structure was maintained in both cases. Larger crystallites in annealed NPs may reduce surface reactivity at higher concentrations, while smaller crystallites in non-annealed NPs could enhance interfacial interactions with bacterial cells. Similar size-dependent effects have been documented for antibacterial nanomaterials.[7]

Further studies should explore how crystallite size independently modulates biofilm inhibition, excluding phase-related variables.

This size dependent biofilm inhibition parallels recent findings. Uthra *et al.*[35] reviewed CuO and ZnO NPs and reported

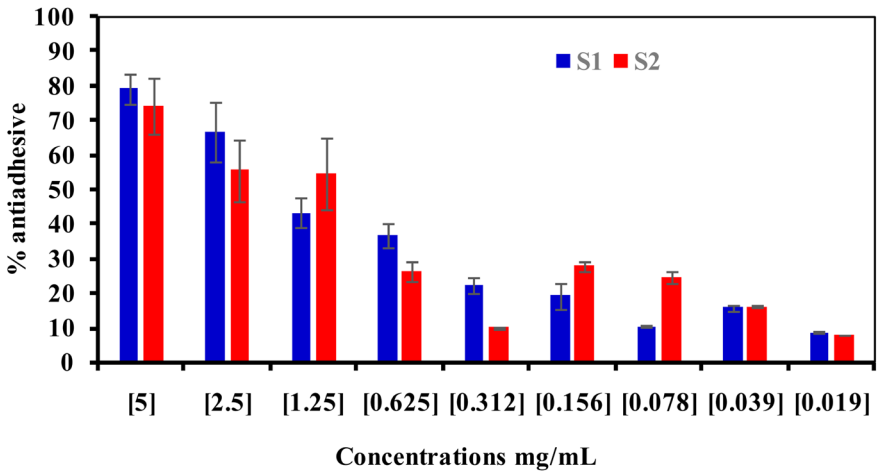

Fig. 6 Antiadhesive activities of S_1 and S_2 NPs at various concentrations ranged between, 19 μg mL^{-1} to 5 mg mL^{-1}.

strong antibiofilm efficacy against antibiotic-resistant bacteria, noting that smaller sizes correlate with higher antimicrobial action due to increased surface area and ROS generation. Similarly, Oetiker *et al.*[36] demonstrated that Cu NPs effectively inhibited oral bacteria biofilms, with efficacy linked to particle size and dispersion. These results align with our observation that non annealed NPs with smaller crystallites outperform at higher concentrations, likely due to enhanced membrane interaction and interference with gene expression pathways involved in biofilm development, and inhibition of surface adhesion proteins.

Evaluation of anti-biofilm activity against MRSA *S. aureus* revealed complementary concentration-dependent mechanisms of action. At high concentrations (5 mg mL^{-1}), both formulations showed >70% inhibition, with a slight advantage for S_1 attributable to its smaller crystallite size (8.2 nm *vs.* 30.2 nm for S_2), promoting better EPS matrix penetration.[37] However, at low concentrations ($\leq$0.156 mg mL^{-1}), S_2 unexpectedly exhibited greater efficacy, likely due to increased generation of reactive oxygen species by easily disaggregated CuO NPs favored by the weak dose,[38] as well as more prolonged Cu^{2+} ion release a phenomenon also observed in $CuFe_2O_4$ systems.[39]

These findings position our $Cu_4SO_4(OH)_6$ phase as an adequate candidate combining the efficacy of complex nanocomposites, the stability of annealed oxides, and the production simplicity of single-component systems, thereby opening new avenues for developing broad-spectrum antimicrobial and antibiofilm agents. Further studies should explore crystallite size optimization for targeted applications, along with *in vivo* validation of these promising properties.

6. Conclusion

In this study, we synthesized and characterized two copper-based nanomaterials non-annealed $Cu_4SO_4(OH)_6$ (note S_1) and annealed CuO (note S_2) and systematically investigated the impact of thermal treatment on their structural, optical, and antibacterial properties. EDS confirmed copper as the primary component, with oxygen and sulfur as secondary constituents. XRD analysis identified monoclinic structures for both phases, with distinct lattice parameters: for the as-prepared S_1 ($a = 5.03$ Å, $b = 8.50$ Å, $c = 11.02$ Å) and after annealing S_2 phase ($a = 4.57$ Å, $b = 3.42$ Å, $c = 5.10$ Å).

Annealing induced a phase transformation from S_2 to S_1, accompanied by a sevenfold increase in crystallite size (8.20 nm to 30.2 nm) and a sharp reduction in specific surface area (114.16 $m^2\ g^{-1}$ to 29.58 $m^2\ g^{-1}$). Optically, the band gap narrowed significantly (2.97 eV to 1.45 eV), while Urbach energy and steepness parameter trends confirmed improved crystallinity, suggesting enhanced electronic properties post-annealing.

Despite its lower surface area, CuO retained notable antibacterial activity, whereas the non-annealed S_2 exhibited superior efficacy (MIC = 0.31–2.5 mg mL^{-1}), attributed to its higher surface reactivity and unique structural features.

Both materials demonstrated strong, dose-dependent anti-adhesive effects against MRSA, with the intermediate phase S_2 showing exceptional performance at higher concentrations.

These results highlight the dual significance of thermal processing: it optimizes structural and electronic properties while unexpectedly revealing the untapped potential of non-annealed copper phases for antimicrobial applications. Future work could explore hybrid systems combining the advantages of both phases for targeted biomedical uses, such as antibacterial coatings or wound dressings.

Building on these findings, future research should prioritize three key directions to advance the translational potential of these materials: quantitative mechanistic studies using DCFH-DA assays and ICP-MS to precisely correlate ROS generation and Cu^{2+} release kinetics with antibacterial efficacy; development of hybrid systems that combine the superior antimicrobial activity of non-annealed S_1 with the enhanced stability of annealed S_2 for applications like smart wound dressings or medical device coatings; and comprehensive *in vivo* validation in clinically relevant infection models to evaluate biofilm penetration and long-term therapeutic effects.

Ethical statement

We, the authors of this manuscript, declare that this work is original, has not been previously published, and is not currently under consideration for publication elsewhere. We confirm that all listed authors have reviewed and approved the manuscript, and that no individuals who meet authorship criteria have been omitted. The order of authors has been agreed upon by all co-authors.

We acknowledge that the Corresponding Author serves as the sole point of contact during the editorial process. They are responsible for communicating with co-authors regarding submission progress, revisions, and final approval of proofs.

Conflicts of interest

The authors declare no competing interests.

Data availability

Raw data are available upon request.

Supplementary information is available. See DOI: **https://doi.org/10.1039/d5ra04198h**.

Acknowledgements

Authors thank the financial support of the Tunisian Ministry of High Education and Scientific Research.

References

1 M. Antonietti and C. Goltner, Superstructures and Functional Materials from Mesophases of Block Copolymers, *Angew. Chem., Int. Ed.*, 1997, **36**, 910–928, DOI: **10.1002/anie.199709101**.

2 N. Wang, H. He and L. Han, Preparation and characterization of ZnO nanorods on Si substrate by hydrothermal method, *Appl. Surf. Sci.*, 2010, **256**, 7335–7338, DOI: **10.1016/j.apsusc.2010.05.057**.
3 Y. Zhang, Z. Liu, D. Zang and L. Feng, Synthesis and characterization of TiO_2 nanoparticles for photocatalytic applications, *Vacuum*, 2014, **9**, 160–165.
4 M. Yurderi, A. Bulut, I. E. Ertas, M. Zahmakiran and M. Kaya, Supported copper nanoparticles on silica for the hydrogenation of unsaturated hydrocarbons, *Appl. Catal., B*, 2015, **165**, 169–175, DOI: **10.1016/j.apcatb.2014.10.011**.
5 W. Chen, H. Zhang, Z. Ma, B. Yang and Z. Li, Recent advances in perovskite solar cells: Efficiency, stability, and large-scale fabrication, *J. Mater. Chem. A*, 2015, **3**, 1–20, DOI: **10.1039/C5TA01234D**.
6 N. Khlifi, S. Mnif, F. Ben Nasr, A. Aifa, H. Guermazi and S. Guermazi, Structural, optical, and antibacterial properties of ZnO nanoparticles synthesized by sol-gel method, *RSC Adv.*, 2022, **12**, 23527–23543, DOI: **10.1039/D2RA02433K**.
7 M. Vincent, P. Hartemann and M. Engels-Deutsch, Antimicrobial applications of copper nanoparticles in healthcare settings, *Int. J. Hyg. Environ. Health*, 2016, **219**, 585–591, DOI: **10.1016/j.ijheh.2016.06.003**.
8 F. Ben Nasr, S. Mnif, H. Guermazi, B. Duponchel, G. Leroy, S. Aifa and S. Guermazi, Structural and optical properties of ZnO nanoparticles doped with transition metals, *J. Cluster Sci.*, 2024, **35**, 1827–1843, DOI: **10.1007/s10876-024-02613-0**.
9 CLSI, *Performance Standards for Antimicrobial Susceptibility Testing, CLSI Supplement M100*, 33rd edn, 2023.
10 J. M. Andrews, Determination of minimum inhibitory concentrations, *J. Antimicrob. Chemother.*, 2001, **48**(Suppl 1), 5–16, DOI: **10.1093/jac/48.suppl_1.5**.
11 EUCAST, Breakpoint Tables for Interpretation of MICs and Zone Diameters, *Version 10.0*, 2020.
12 T. J. Mason and J. P. Lorimer, Applied Sonochemistry: Uses of Power Ultrasound in *Chemistry and Processing*, Wiley-VCH, Weinheim, 2002.
13 K. S. Suslick, Sonochemistry, in *Kirk-Othmer Encyclopedia of Chemical Technology*, ed. J. I. Kroschwitz, Wiley, New York, 4th edn, 1998, vol. 26, pp. 516–541.
14 M. Jardak, A. Atoissi, D. Msalbi, D. Atoui, B. Bouizgarne, G. Rigane, R. Ben Salem, S. Aifa and S. Mnif, Antibacterial and antibiofilm activities of Laurus nobilis L. essential oil against Staphylococcus aureus and Pseudomonas aeruginosa, *Microb. Pathog.*, 2022, **164**, 105449, DOI: **10.1016/j.micpath.2022.105449**.
15 F. Elghali, D. Msalbi, F. Frikha, M. Alonazi, E. Sahli, B. Hakim, S. Mnif, A. Ben Bacha and S. Aifa, Green synthesis of silver nanoparticles using Peganum harmala extract: Characterization, antimicrobial activity, and cytotoxicity evaluation, *ACS Omega*, 2024, **9**, 48112–48124, DOI: **10.1021/acsomega.4c01234**.
16 S. Vilminot, M. Richard-Plouet, G. Andre, D. Swierczynski, M. Guillot, F. Bouree-Vigneron and M. Drillon, Layered organic-inorganic materials: Structure and magnetic properties of copper(II) aminoalkylphosphonates, *J. Solid State Chem.*, 2003, **170**, 255–264, DOI: **10.1016/S0022-4596(02)00022-3**.
17 K. Martin and G. McCarthy, *et.al*, Crystal structure of barium copper silicate, *J. Solid State Chem.*, 1990, **89**, 184.
18 W. Jia, E. Reitz, H. Sun, H. Zhang and Y. Lei, Synthesis and characterization of ZnO nanorod arrays *via* solution deposition, *Mater. Lett.*, 2009, **63**, 519–522, DOI: **10.1016/j.matlet.2008.11.037**.
19 S. Singhal, J. Kaur, T. Namgyal and R. Sharma, Structural and magnetic properties of Co1-xZnxFe2O4 nanoparticles prepared by sol-gel auto-combustion method, *Physica B*, 2012, **407**, 1223–1226, DOI: **10.1016/j.physb.2012.01.103**.
20 G. K. Williamson and W. H. Hall, X-ray line broadening from filed aluminium and wolfram, *Acta Metall.*, 1953, **1**, 22–31, DOI: **10.1016/0001-6160(53)90006-6**.
21 S. Kahraman, H. A. Çetinkara, F. Bayansal, H. M. Çakmak and H. S. Güder, Structural and optical properties of ZnO thin films prepared by sol-gel method, *Philos. Mag.*, 2012, **92**, 2150–2163, DOI: **10.1080/14786435.2012.669064**.
22 B. K. Ku and P. Kulkarni, Measurement of surface area of fine particles using diffusion charging and mobility analysis, *J. Aerosol Sci.*, 2012, **47**, 100–110, DOI: **10.1016/j.jaerosci.2012.01.002**.
23 K. Nakamoto, *Infrared and Raman Spectra of Inorganic and Coordination Compounds*, Wiley, Hoboken, 6th edn, 2009.
24 R. L. Frost, J. T. Kloprogge, S. C. Russell and J. L. Szetu, Vibrational spectroscopy of the phosphate mineral lazulite $MgAl_2(PO_4)_2(OH)_2$, *Spectrochim. Acta, Part A*, 2006, **63**, 1–8.
25 V. C. Farmer, *The Infrared Spectra of Minerals*, Mineralogical Society, London, 1974.
26 S. Huo, Y. Jiang, A. Gupta, Z. Jiang, R. F. Landis, S. Hou, X. J. Liang and V. M. Rotello, Fully Zwitterionic Nanoparticle Antimicrobial Agents through Tuning of Core Size and Ligand Structure, *ACS Nano*, 2016, **27**, 8732–8737, DOI: **10.1021/acsnano.6b04207**.
27 M. Amiri, Z. Etemadifar, A. Daneshkazami and M. Nateghi, Antibacterial activity of dental adhesives containing nanoparticles, *J. Dent.*, 2017, **4**, 347–352.
28 M. Agarwala, B. Choudhury and R. N. S. Yadav, Antimicrobial activity of silver nanoparticles against clinical isolates, *Indian J. Microbiol.*, 2014, **54**, 365–368, DOI: **10.1007/s12088-014-0462-z**.
29 A. Azam, *et al.*, Antimicrobial activity of metal oxide nanoparticles against Gram-positive and Gram-negative bacteria: A comparative study, *Int. J. Nanomedicine*, 2012, **7**, 6003–6009, DOI: **10.2147/IJN.S35347**.
30 S. V. Gudkov., D. E. Burmistrov, P. A. Fomina, S. Z. Validov and V. A. Kozlov, Antibacterial Properties of Copper Oxide Nanoparticles, *Int. J. Mol. Sci.*, 2024, **25**, 11563, DOI: **10.3390/ijms252111563**.
31 S. M. Javadhesari, S. Alipour, S. Mohammadnejad and M. R. Akbarpour, Antibacterial activity of ultra-small copper oxide (II) nanoparticles synthesized by mechanochemical processing against S. aureus and E. coli, *Mater Sci Eng C Mater Biol Appl*, 2019, **105**, 110011, DOI: **10.1016/j.msec.2019.110011**.

32 A. Azam, A. S. Ahmed, M. Oves, M. S. Khan and A. Memic, Size-dependent antimicrobial properties of CuO nanoparticles against Gram-positive and -negative bacterial strains, *Int. J. Nanomedicine.*, 2012, **7**, 3527–3535, DOI: **10.2147/IJN.S29020**.

33 T. Khairy, D. H. Amin, H. M. Salama, *et al.*, Antibacterial activity of green synthesized copper oxide nanoparticles against multidrug-resistant bacteria, *Sci. Rep.*, 2024, **14**, 25020, DOI: **10.1038/s41598-024-75147-0**.

34 J. D. Moore, A. Avellan, C. W. Noack, Y. Guo, G. V. Lowry and K. B. Gregory, Time-dependent bacterial transcriptional response to CuO nanoparticles differs from that of Cu^{2+} and provides insights into CuO nanoparticle toxicity mechanisms, *Environ. Sci. Nano*, 2017, **4**, 2321–2335, DOI: **10.1039/EN00600D**.

35 C. Uthra, K. Nagaraj, M. A. Wadaan, C. Karuppiah, P. Maity, A. Baabbad, R. Kaliyaperumal, R. Venkatachalapathy, F. Shah and P. Kumar, Zinc and Copper Oxide Nanoparticles: Pioneering Antibacterial and Antibiofilm Strategies for Environmental Restoration against Antibiotic-Resistant Bacteria, *Materials*, 2024, **17**(14), 3444, DOI: **10.3390/ma17143444**.

36 N. Oetiker, D. Salinas, J. Lucero-Mora, R. Orellana, M. Quiroz-Muñoz, D. Bravo and J. M. Pérez-Donos, Antimicrobial Effect of Copper Nanoparticles on Relevant Supragingival Oral Bacteria, *Microorganisms*, 2024, **12**(3), 624, DOI: **10.3390/microorganisms12030624**.

37 Q. Wang, F. Kang, Y. Gao, *et al.*, Sequestration of nanoparticles by an EPS matrix reduces the particle-specific bactericidal activity, *Sci. Rep.*, 2016, **6**, 21379, DOI: **10.1038/srep21379**.

38 C. Angelé-Martínez, K. V. Nguyen, F. S. Ameer, J. N. Anker and J. L. Brumaghim, Reactive oxygen species generation by copper(II) oxide nanoparticles determined by DNA damage assays and EPR spectroscopy, *Nanotoxicology*, 2017, **11**(2), 278–288, DOI: **10.1080/17435390.2017.1293750**.

39 R. Quezada, Y. Quintero, J. C. Salgado, H. Estay and A. García, Understanding the Phenomenon of Copper Ions Release from Copper-Modified TFC Membranes: A Mathematical and Experimental Methodology Using Shrinking Core Model, *Nanomaterials*, 2020, **10**, 1130, DOI: **10.3390/nano10061130**.